Advances in Magnetics

Co–Fe Metal/Native-Oxide Multilayers: A New Direction in Soft Magnetic Thin Film Design II. Microscopic Characteristics and Interactions

G. S. D. Beach[1] and A. E. Berkowitz[2]

[1]Department of Physics, University of Texas at Austin, Austin, TX 78712-1081 USA
[2]Department of Physics and the Center for Magnetic Recording Research, University of California at San Diego, La Jolla, CA 92093-0401 USA

Co_xFe_{100-x} metal/native-oxide multilayer (MNOM) films exhibit soft magnetic properties, large magnetization, high resistivity, and a potential operating bandwidth of several gigahertz. These attractive characteristics are facilitated by ultrathin magnetic native oxide layers introduced to provide a high-resistivity barrier between nanocrystalline metal layers while preserving interlayer coupling and contributing to the net moment. This paper addresses several important features of the MNOM system from a microscopic perspective. The uniaxial anisotropy of MNOM thin films is discussed in detail and "exchange averaging" is invoked to account for its vanishingly small effective dispersion. The role of the native oxide in establishing interlayer exchange coupling is demonstrated, and a detailed account of the nature of the oxide is presented. In the Fe MNOM system, the oxide is shown to have a volume-averaged magnetization of 732(35) emu/cm^3, with a temperature dependence comparable to that of metallic Fe. The magnetism of this largely "interfacial" oxide is supported by the metal and collapses in the absence of the metal. The oxide retains a large net moment for Co fractions up to at least $x = 50$, but oxide magnetism is lost at high Co fractions, coinciding with the loss of soft magnetic properties.

***Index Terms*—Magnetic multilayers, magnetic recording, magnetic shielding, magnetodynamics, permeability, soft magnetic materials.**

I. Introduction

RECENT work has demonstrated the promise of a new Co_xFe_{100-x} metal/native-oxide multilayer (MNOM) composite for use in gigahertz-bandwidth shielding applications [1]–[3]. The MNOM structure consists of nanogranular high-moment Co_xFe_{100-x} metal layers separated by high-resistivity magnetic native oxide layers of nanometer thickness. Over a wide range of alloy composition and structural parameters, MNOM thin films exhibit soft magnetic properties, a large saturation magnetization, and favorable high-frequency characteristics. The preceding paper [3] described the fabrication and microstructure of this system and provided a detailed review of the macroscopic magnetic characteristics that make it a serious candidate for high-frequency applications in magnetic recording and telecommunications. The present paper attempts to explain some of those properties by addressing their microscopic origins.

A particularly striking feature of the Co_xFe_{100-x} MNOM system is the remarkably low dispersion of the deposition field-induced uniaxial anisotropy, which ranges in magnitude from $\sim$10 Oe to over 200 Oe depending on alloy composition, x. In Section II, we discuss possible sources of local anisotropy in this system and describe how the "exchange averaging" of a preferentially oriented distribution of locally varying anisotropy over a comparatively large exchange-coupled volume would lead to such small effective dispersion.

A fuller understanding of the macroscopic magnetic properties of the MNOM system requires a detailed description of the properties of the constituent metal and oxide layers and their interactions. Section III characterizes the magnetism and stoichiometry of the predominantly "interfacial" oxide layers found in MNOM films, and Section IV demonstrates exchange coupling between these oxide layers and the metal that surrounds them. A surprising picture emerges from this study. The native oxide in the Fe MNOM system has the stoichiometry of FeO, which, in the bulk, is an antiferromagnet with an ordering temperature of 197 K. However, this nanoscale *buried* native oxide orders well above room temperature, with a volume-averaged magnetization exceeding that of Fe_3O_4 by $\sim$40% and of γ-Fe_2O_3 by $\sim$90%. The magnetism of the native Fe oxide, all of whose spins are either directly or indirectly coordinated by metallic Fe, is supported by the metal and collapses in the absence of the metal. Oxide magnetism is preserved in the Co_xFe_{100-x} MNOM system for Co fraction up to at least $x = 50$; magnetism is lost at high Co fractions ($x > 90$), coinciding with the loss of soft magnetic properties.

Co_xFe_{100-x} MNOM thin films have been prepared [3] by alternately depositing thin Co_xFe_{100-x} alloy layers (typically a few nanometers) and exposing them *in situ* to a low partial pressure of O_2 to form metal/native-oxide bilayers. The

Digital Object Identifier 10.1109/TMAG.2005.847630

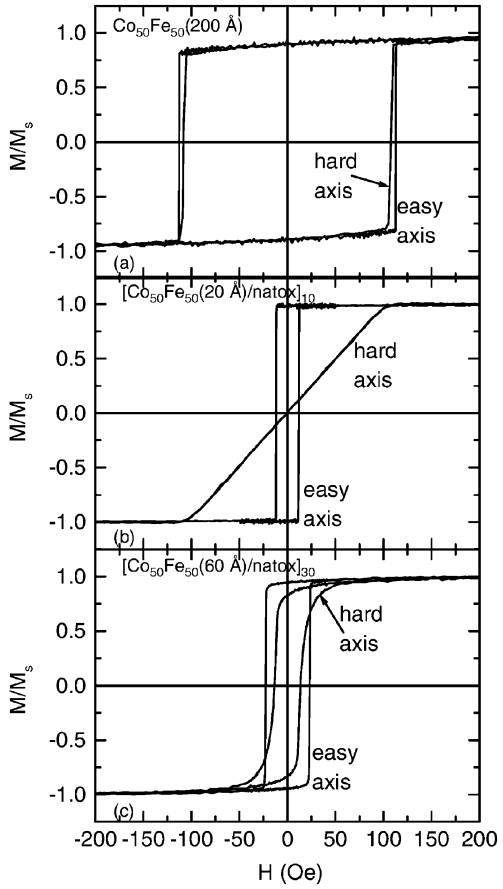

Fig. 1. Normalized in-plane hysteresis loops measured along (easy) and orthogonal to (hard) the deposition field direction for (a) $Co_{50}Fe_{50}$(200 Å) and (b) $[Co_{50}Fe_{50}(20\ \text{Å})/\text{natox}]_{10}$, and (c) $[Co_{50}Fe_{50}(60\ \text{Å})/\text{natox}]_{30}$.

notation $[Co_xFe_{100-x}(t_0)/\text{natox}]_N$ describes a MNOM with N metal/native-oxide bilayers, each formed by subjecting a Co_xFe_{100-x} metal layer of thickness t_0 to an O_2 exposure of $\sim 8 \times 10^{-5}$ Torr for 10 s. This exposure oxidizes a thickness t_{ox} of metal per layer ranging from ~ 8.4 Å for $x = 0$ (pure Fe) to ~ 6.3 Å for $x = 90$ [3].

Metal layers were dc sputter-deposited at room temperature using Co_xFe_{100-x} alloy targets. Si(100) substrates covered by a thin (~ 30 Å) native Si oxide were used unless otherwise noted, and films were capped with ~ 100 Å of SiO_2 to protect against further oxidation. A dc magnetic field (~ 100 Oe) was applied in the film plane during deposition, establishing the easy axis of the uniaxial anisotropy described below.

II. Anisotropy and Coercivity in the MNOM System

A. Hysteresis Characteristics

Fig. 1(a) and (b) illustrates two important changes in hysteresis loop characteristics achieved by the suitable introduction of periodic native oxide layers into a $Co_{50}Fe_{50}$ film. The first is a substantial drop in coercivity (H_c), from over 100 Oe in a continuous 200 Å $Co_{50}Fe_{50}$ film to ~ 10 Oe in a corresponding MNOM, $[Co_{50}Fe_{50}(20\ \text{Å})/\text{natox}]_{10}$. Second, the nearly isotropic in-plane field response of the continuous film gives way in the MNOM to a strong uniaxial anisotropy with remarkably low dispersion, as inferred from the almost perfectly closed and linear hard-axis loop and square easy-axis loop. As shown in [3], similar results are obtained in $[Co_xFe_{100-x}(20\ \text{Å})/\text{natox}]_N$ films from $x = 0$ to at least $x = 90$, with soft properties lost only in the pure Co limit. Over a broad range of x, such films have a composition-independent H_c of ~ 10 Oe and hard-axis loops that are closed or nearly so. Importantly, the anisotropy field H_k depends strongly on x, increasing almost linearly from ~ 10 to ~ 220 Oe as x increases from 0 to 90.

Continuous $Co_{50}Fe_{50}$ films similar to that of Fig. 1(a) have typical grain sizes of several hundred angstroms [4]. The emergence of soft magnetic properties in going to a MNOM structure are accompanied by a reduction in metal grain size to several nanometers, as seen in transmission electron micrograph (TEM) cross sections [1], [3] for $t_0 = 20$ Å. The soft properties degrade when t_0, and presumably the average grain size, becomes too large [3]. As t_0 increases from 20 to 60 Å for $Co_{50}Fe_{50}$ MNOMs [Fig. 1(c)], the hysteresis loops along and orthogonal to the deposition field axis become less distinct, each showing considerable hysteresis. We suggest that the low dispersion uniaxial anisotropy in low-t_0 MNOM films may arise from the "exchange-averaged" single-ion anisotropy of the Co^{2+} in the oxide layers, and that the transition in hysteresis characteristics with increasing t_0 is due to the increasing dominance of randomly oriented magnetostrictive anisotropy of Co_xFe_{100-x} when the metallic grain size approaches the domain wall width.

B. Exchange Averaging

The properties of many nanocrystalline soft magnetic materials and composites [5]–[9], including MNOMs [1], [10], have inaccurately been ascribed to the random-anisotropy (RA) model of Hertzer [11]. The assumptions in the Hertzer RA model lead to a vanishing anisotropy, whereas the MNOM system, as with all soft materials appropriate for high-frequency applications, has a strong uniaxial anisotropy. Though the Hertzer RA model is thus inappropriate for these systems, the notion of "exchange averaging" a distribution of local anisotropies over the exchange-coupled volume is important. If exchange coupling is sufficient to cause the adjacent moments in a macroscopic region to follow each other rather than the local anisotropy, the effective anisotropy is the *average* of the local anisotropy within that region.

The essential difference between a random anisotropy model and more general distributed anisotropy models such as "ripple" models [12], is that a diverging exchange length yields an effective anisotropy converging to zero in the former but to a finite value in the latter. It is the effective dispersion of the anisotropy, not its magnitude, that decreases with increasing exchange length. A nonuniform material with local uniaxial anisotropy energy density of magnitude $K_u(\vec{r})$ and easy direction (axis) $\vartheta(\vec{r})$ that vary with position $\vec{r}$ has a local anisotropy energy density

$$E_a(\vec{r}) = -K_u(\vec{r}) \cos^2[\theta(\vec{r}) - \vartheta(\vec{r})]. \quad (1)$$

Here, θ and ϑ are the angles of the local magnetization and local easy axis, respectively, referenced to a fixed global axis. If the

angular dispersion of the local anisotropy axis has a distribution $\eta(\vartheta)$ (which can be redefined to account for a distribution in the magnitude of K_u) the volume average of (1) over a region of uniform $\theta(\vec{r}) = \theta$ (e.g., for an exchange-coupled volume $V_{\rm ex}$) becomes (omitting constants)

$$\langle E_a \rangle_V = -K_u \int \eta(\vartheta) \cos^2(\theta - \vartheta) d\vartheta = -\bar{K}_u \cos^2(\theta - \alpha) \tag{2}$$

where

$$\alpha = \frac{1}{2} \tan^{-1}\left(\frac{B}{A}\right); \quad \bar{K}_u = \frac{A}{\cos(2\alpha)} K_u \tag{3}$$

and

$$A = 1 - 2\int \eta(\vartheta) \sin^2(\vartheta)\, d\vartheta;$$
$$B = -2\int \eta(\vartheta) \sin(\vartheta)\cos(\vartheta) d\vartheta. \tag{4}$$

Equation (2) simply states that the volume-averaged anisotropy energy density for any arbitrary collection of local uniaxial anisotropies (i.e., $\eta(\vartheta)$) is likewise uniaxial. Note that $\bar{K}_u \to 0$ for a uniform (random) distribution $\eta(\vartheta)$, and the special case of the Hertzer RA model [11] is recovered. More generally, A and B contain the symmetric and antisymmetric components, respectively, of the anisotropy distribution $\eta(\vartheta)$. An ensemble of finite sampling volumes V will yield a distribution in A and B, and thus in α and $\bar{K}_u$. It is the asymmetric statistical fluctuations in a finite sampling of $\eta(\vartheta)$ over a finite exchange-coupled volume that determine the effective directional anisotropy dispersion, $\sqrt{\langle \alpha^2 \rangle}$.

As an example, a purely Gaussian dispersion $\eta(\vartheta)$ with width $\sigma \ll 1$ gives a volume-averaged anisotropy of $E_a = -K_u(1 - 2\sigma^2)\cos^2(\theta) = -\bar{K}_u \cos^2(\theta)$ with an effective angular dispersion $\sqrt{\langle \alpha^2 \rangle} = \sigma/\sqrt{N}$, where $N = V_{\rm ex}/\delta^3$. Here, $V_{\rm ex}$ is the exchange-coupled volume ($V_{\rm ex} \sim \sqrt{A/\bar{K}_u}$ for exchange stiffness constant A), and δ is the length scale for variations in ϑ. Importantly, for a nonuniform distribution, $\bar{K}_u$ does not vanish with decreasing δ, which would further increase $V_{\rm ex}$ as per the Hertzer RA model. Instead, it is the *width* of the distribution that vanishes.

C. Angular Dependence and Anisotropy Dispersion

The angular dependence of the saturation torque and of $M(H)$ loops provide complimentary means to characterize the uniaxial anisotropy and its angular dispersion. The saturation torque provides a measure of the anisotropy energy, (1), averaged over the film volume. At saturation, the torque density (L) is given by

$$L = -\frac{\partial E}{\partial \theta} = \bar{K}_u \sin(\theta). \tag{5}$$

A torque curve of a $[Co_{50}Fe_{50}(20\ \text{Å})/\text{natox}]_{10}$ film measured at $H = 3$ kOe ($\gg H_k$) is shown and fitted by (5) in Fig. 2. The data are purely uniaxial with $\bar{K}_u = 7.9 \times 10^4$ erg/cm^3, yielding an anisotropy field $H_k = 2\bar{K}_u/\bar{M}_s = 102(5)$ Oe using an independently measured value for $\bar{M}_s$. This quantity is somewhat larger than but statistically consistent with the value 92 Oe estimated from the hard axis loop of this sample, shown in Fig. 1(b).

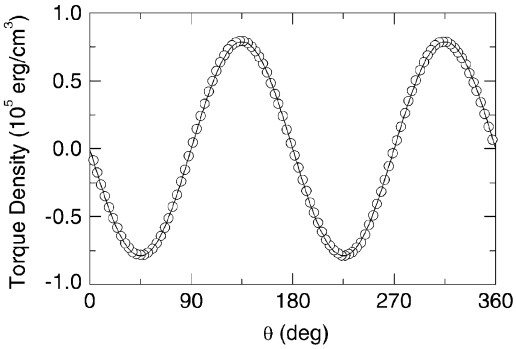

Fig. 2. Torque curve measured at $H = 3$ kOe (open circles) and fit (solid line) for a $[Co_{50}Fe_{50}(20\ \text{Å})/\text{natox}]_{10}$ film.

The saturation torque is insensitive to dispersion in the local anisotropy, integrating any random anisotropy to zero and any preferentially oriented anisotropy to a single uniaxial term. However, the low-field and remanent characteristics of hysteresis loops are influenced by dispersion; they are determined by the exchange-averaged local anisotropy in the system. Easy-axis dispersion would cause the remanent magnetization to "fan out" along the distributed local easy axes. Effective angular dispersion [i.e., (3)] on a length scale larger than the domain size would reduce M_r/M_s near the nominal easy axis and increase it near the nominal hard axis. An effective angular dispersion of Gaussian width $\sigma \ll 1$ would yield easy- and hard-axis remanence ratios of $1 - \sigma^2/2$ and σ, respectively. Likewise, the coercivity along the nominal hard axis would increase as $H_c^{\rm hard} = \sigma H_k$.

The hysteresis loops of $[Co_{50}Fe_{50}(20\ \text{Å})/\text{natox}]_N$ exhibit an extremely low effective anisotropy dispersion, indicating nearly complete "exchange averaging" in this system. The angular dependence of these loops is almost perfectly described by a single-domain Stoner–Wolforth (SW)-like rotational model [13] with zero dispersion, with the addition of a sharp nucleation field that "shorts out" rotational switching, which occurs at $H_c = H_k$ in the SW model [13].

Fig. 3(a) contains $M(H)$ loops for several measuring angles θ from the easy axis. The angular dependence of the remanent ratio M_r/M_s, plotted in Fig. 3(b), is well-fitted by a single term in $\cos(\theta)$ with a coefficient of unity; the magnetization uniformly rotates toward a single, well-defined uniaxial easy axis regardless of the direction of saturation.

The coercivity H_c, defined as the magnetization zero-crossing field, is due to domain wall mediated reversal near the easy axis and uniform rotation near the hard axis. Along the easy axis, switching occurs at a critical (wall nucleation) field H_0. As θ increases from 0, H_c increases in a fashion typical of domain wall displacement [13], i.e.,

$$H_c^{\rm dw} = \frac{H_0}{\cos(\theta)}. \tag{6}$$

A domain wall (or walls) sweeps across the sample when the easy-axis component of H reaches the critical field H_0. This relation adequately describes the angular dependence of the coercive field within a range $\sim 70^\circ$ of the easy axis, as seen in Fig. 3(c).

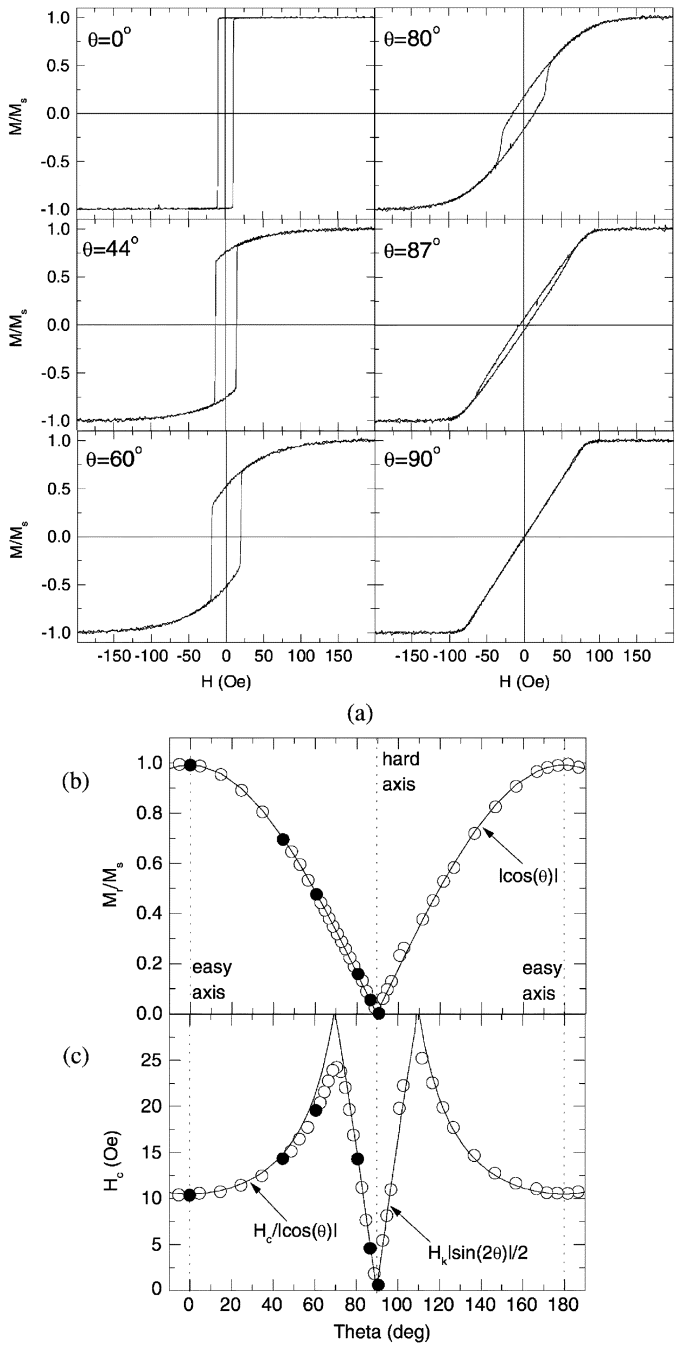

Fig. 3. (a) Hysteresis loops of $[Co_{50}Fe_{50}(20\ \text{Å})/\text{natox}]_{50}$ measured at various angles θ with respect to the easy axis. The angular dependence of the remanent magnetization ratio and coercivity are plotted in (b) and (c), respectively. Solid lines are fits to the indicated functions (see text).

The decrease (increase) of M with decreasing (increasing) fields that occurs before critical magnetization switching is due to reversible rotation, with $\vec{M}$ rotating to minimize the free energy

$$E = -K_u \cos^2(\phi - \theta) - M_s H \cos(\phi) \tag{7}$$

where the applied field H makes angles θ and ϕ with the easy axis and the magnetization, respectively. Near the hard axis, reversible rotation occurs over a wide enough field range to allow the magnetization zero crossing field to occur in the reversible region, as seen in the $M(H)$ loop measured at $\theta = 80°$ [Fig. 3(a)].

At fields less than H_c^{dw}, the projection of $\vec{M}$ along the field (measuring) axis, $M_s \cos(\phi)$, will cross zero when $\phi = 90°$. From (7), the field corresponding to this condition is

$$H_c^{\text{rot}} = \frac{H_k |\sin(2\theta)|}{2}. \tag{8}$$

Thus, for a given measuring angle θ, the zero-crossing field H_c is given by the minimum of the zero-crossing fields for domain-wall reversal (6) and reversible rotation (8). The angular dependence of H_c follows this behavior closely, as seen in Fig. 3(c). The best fit of $H_c(\theta)$ near the hard axis using (8) gives $H_k = 87(2)$ Oe, agreeing with the value 88 Oe estimated from the corresponding hard-axis loop in Fig. 3(a). The "rounding" near the point $H_c^{\text{rot}} = H_c^{\text{dw}}$ may be explained by a finite critical switching field distribution about H_0, which, like H_c^{dw}, increases as $\sim 1/\cos(\theta)$. The data of Fig. 3 provide an upper limit to the angular dispersion of the effective anisotropy within the sample. The minimum coercivity and remanence ratios measured near the hard axis for this MNOM limit the effective angular anisotropy dispersion to $\sigma < 0.4°$.

D. Local Anisotropy

Exchange averaging as described above provides a mechanism for obtaining low-dispersion uniaxial anisotropy, given a source of local anisotropy with a distribution tending toward a preferential axis. We suggest that in the MNOM system, this source may be preferentially oriented single-ion anisotropy of Co^{2+} in the oxide layers. Both the saturation magnetostriction and the magnetocrystalline anisotropy of the Co_xFe_{100-x} alloys vary strongly with x ; the former crosses zero near $x = 5$ and $x = 90$ and is maximum near $x = 50$ [14], at which composition the latter crosses zero [14]. It is therefore difficult to explain the observed linear increase in H_k with x in the MNOM system through either stress-induced magnetostrictive anisotropy or magnetocrystalline anisotropy of the metal. Alternatively, directional (pair-ordering) anisotropy has been used to explain the field-induced uniaxial anisotropy of binary alloys such as Permalloy. However, the magnitude expected for such an anisotropy (H_k of several oersteds) is much smaller than the values in the MNOM system (H_k up to $\sim$200 Oe). Furthermore, any magnetic anisotropy resulting from directionally anisotropic pairing of Co–Co, Fe–Fe, or Co–Fe would necessarily vanish in the Co-rich and Fe-rich limits. Rather, the approximately linear increase of H_k with x over the full range of x implies an anisotropy energy density proportional to the density of Co in the system, suggesting single-atom or single-ion anisotropy as the source. Co^{2+} possesses a large single-ion anisotropy due to its large unquenched angular momentum [13], [15]: octahedrally coordinated Co^{2+} has a uniaxial anisotropy along the trigonal $\langle 111 \rangle$ direction. A small preferential occupation by Co^{2+} of octahedral sites with $\langle 111 \rangle$ closer to the deposition field axis during growth could therefore be an important anisotropy source.

In the MNOM system, even a small tendency of the local anisotropy to orient toward the deposition field axis could yield

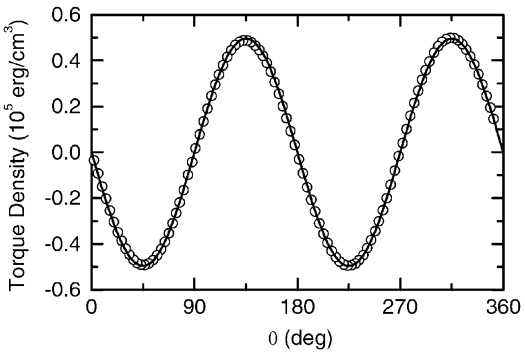

Fig. 4. Torque curve measured at $H = 3$ kOe (open circles) and fit (solid line) for a $[Co_{50}Fe_{50}(60\ \text{Å})/\text{natox}]_{30}$ film.

a net low-dispersion uniaxial anisotropy, if the exchange length were much greater than the length scale of local dispersion. If the dominant source of local anisotropy in the MNOM system were due to Co^{2+}, that length scale would be the average Co^{2+} spacing (∼several angstroms), which is much less than typical exchange lengths (hundreds of angstroms) in soft magnetic films. Exchange averaging could evidently yield a nearly dispersion-free effective uniaxial anisotropy in $Co_{50}Fe_{50}$ MNOMs with sufficiently low t_0. However, the uniaxial anisotropy evident in both the hysteresis loops and the torque curves of MNOMs with small t_0 is still present in the thicker- t_0 MNOMs that lack highly anisotropic hysteresis characteristics. This uniaxial anisotropy is clearly evident in the saturation torque data of Fig. 4 for the $[Co_{50}Fe_{50}(60\ \text{Å})/\text{natox}]_{30}$ MNOM of Fig. 1(c), despite the loss of the clear distinction between the "easy"- and "hard"-axis hysteresis loops of Fig. 1(c) for this sample. The uniaxial torque curves for $t_0 = 20$ Å and $t_0 = 60$ Å differ only in magnitude, with that of the latter lower by ∼35% compared to the former. Such a decrease in $\bar{K}_u$ would be qualitatively expected if the uniaxial anisotropy originated in the oxide, whose volume fraction decreases with increasing t_0. The contrast between the uniaxial saturation torque curve and the hysteresis loops for MNOMs with thicker t_0 suggests an anisotropy term whose volume average is either uniaxial or close to zero, but which has a large local dispersion that is not effectively exchange averaged over the exchange-coupled volume.

The composition dependence of the coercivity of continuous Co_xFe_{100-x} films [1] closely follows that of the saturation magnetostriction [14], and is maximum near $x = 50$. For randomly oriented grains, stresses within the film would yield randomly oriented anisotropy on the length scale of the grain size. It is well-known that the coercivity of large-magnetostriction Co_xFe_{100-x} films drops dramatically when the grain size falls below the domain wall width [4], [16]. The degradation in the hysteresis characteristics with increasing t_0 for the MNOM films could therefore be explained by a random anisotropy contribution by magnetostriction that becomes important when t_0, and thus the Co_xFe_{100-x} grain sizes, exceeds a critical value. At low t_0, the exchange length exceeds the metal grain size, and the exchange-averaging of this random anisotropy component reveals the uniaxial term that exists but is "masked" at thicker t_0.

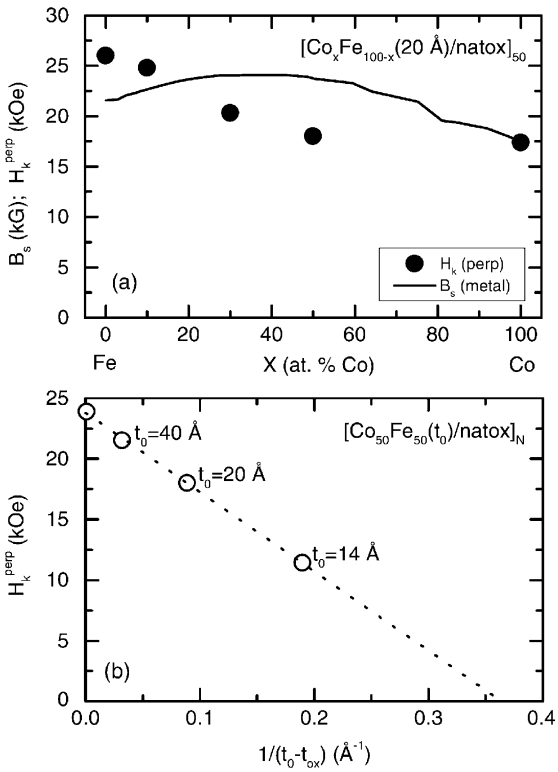

Fig. 5. (a) Perpendicular anisotropy field for $[Co_xFe_{100-x}(20\ \text{Å})/\text{natox}]_{50}$ films versus composition, compared with B_s of bulk Co_xFe_{100-x}. (b) Perpendicular anisotropy field for $[Co_{50}Fe_{50}(t_0)/\text{natox}]_N$ films of several t_0 (with $Nt_0 \sim 1000$ Å) plotted against the inverse nominal metal layer thickness (see text; point at $1/(t_0 - t_{ox}) = 0$ is $4\pi_s$ of bulk $Co_{50}Fe_{50}$).

E. Interface Anisotropy

In [3], it was stated that the perpendicular anisotropy fields of several MNOM films differed from the values expected from demagnetizing field contributions. In general, the perpendicular anisotropy field in the thin film limit is

$$H_k^{\perp} = 4\pi M_s - H_s \tag{9}$$

where $4\pi M_s$ is the demagnetizing field and

$$H_s = 2K_s/M_s\delta \tag{10}$$

accounts for possible thickness (δ)-dependent surface or interface anisotropy (K_s).

$H_k^{\perp}$ was taken from hysteresis loops measured normal to the film plane using a superconducting quantum interference device (SQUID) magnetometer. The results for several $[Co_xFe_{100-x}(20\ \text{Å})/\text{natox}]_{50}$ films of varying x are plotted in Fig. 5(a), and are compared with $4\pi M_s^{\text{bulk}}$ for the corresponding bulk metal alloy. The metal magnetization, being ∼2.5–3 times larger than that of the oxide (see Section III), provides the dominant demagnetizing field and sets an upper limit on the demagnetizing field contribution to $H_k^{\perp}$. The data of Fig. 5(a) show a discrepancy between $H_k^{\perp}$ and $4\pi M_s^{\text{bulk}}$ for all but the pure Co MNOM. Fig. 5(b) points to interfacial anisotropy as the origin of this discrepancy. In that figure, the decrease of $H_k^{\perp}$ with decreasing layer thickness t_0 for a set of $[Co_{50}Fe_{50}(t_0)/\text{natox}]_N$ films follows (9), where $M_s = 1890$ emu/cm^3 is the saturation magnetization of bulk $Co_{50}Fe_{50}$ and H_s is given by (10). The surface term decreases as $1/(t_0 - t_{ox})$

with a best-fit value $t_{\rm ox} = 8.5$ Å. $t_{\rm ox}$ is thus identified as the nominal thickness of metal that oxidizes per layer during O_2 exposure, independently measured as 7(1) Å in [10]. The slope of the data in Fig. 5(b) gives an interface anisotropy $K_s = 0.65(4)$ erg/cm^2 for this range of t_0 (which, for comparison, is comparable to the interface anisotropy observed in Co/Pd superlattices [17]).

The origin of the large K_s in this system is not clear. However, we make two remarks on its implications. First, there is a crossover from $H_k^{\perp} > 4\pi M_s^{\rm bulk}$ to $H_k^{\perp} < 4\pi M_s^{\rm bulk}$ near $x = 10$, indicating a change in sign of the anisotropy from negative (easy plane) to positive (easy axis) with increasing x. For $H_k^{\perp} < 4\pi M_s^{\rm bulk}$, the interface anisotropy should lower the precessional frequency due the proportionality of $f_{\rm FMR}$ to $\sqrt{M_{\rm eff}}$. However, for the most Fe-rich compositions, the interface anisotropy *augments* the demagnetizing field, offering the possibility of surpassing the Snoek limit [18] on bandwidth versus permeability. Interestingly, there is no evidence for interfacial anisotropy in the pure Co MNOM.

We also note that extrapolation of the data in Fig. 5(b) predicts that the interface anisotropy would exceed the demagnetizing field for a $Co_{50}Fe_{50}$ MNOM with metal/oxide bilayers containing <3 Å of metal, or $t_0 < 11$ Å. This raises the intriguing but unexplored possibility that for certain Co_xFe_{100-x} compositions, the MNOM could display net perpendicular anisotropy in the ultrathin metal layer limit.

III. Characteristics of the Buried Native Oxide

An understanding of the behavior of the MNOM system requires defining the nature of the buried native oxide layers. This section presents a characterization of the magnetism and stoichiometry of these predominantly "interfacial" oxide layers.

A. Net Moment

The average net moment $\bar{\mu}_{\rm net}$ of a MNOM is the sum of the net moments of the metal ($\mu_{\rm net}^m$) and oxide ($\bar{\mu}_{\rm net}^{\rm ox}$), weighted by their respective fractions, and may be written

$$\bar{\mu}_{\rm net} = \bar{\mu}_{\rm net}^{\rm ox} + (\mu_{\rm net}^m - \bar{\mu}_{\rm net}^{\rm ox})\, f. \tag{11}$$

The observation of a linear relation between $\bar{\mu}_{\rm net}$ and the atomic metal fraction f [19] permits the net moments of the constituent metal and oxide components to be determined independently from the slope and intercept of (11).

The MNOM system affords a convenient means of varying f by varying t_0. A series of Fe MNOM samples, $[{\rm Fe}(t_0)/{\rm natox}]_N$, was prepared, with t_0 ranging from 5 Å to 60 Å and with N satisfying $Nt_0 \approx 1000$ Å and $N \geq 30$. For each sample, $\bar{\mu}_{\rm net}$ was measured in a SQUID magnetometer and f was determined using conversion electron Mössbauer spectroscopy (CEMS) [19]. CEMS is sensitive to the local magnetic and chemical environments of Fe; the decomposition of a CEMS spectrum into its metal and oxide components permits a precise measure of the fraction of Fe in each chemical state. For the MNOM samples, two sextets were required to account for asymmetric broadening in the metal subspectrum. Fits yielded a hyperfine field (HF) of 330 kOe and an isomer shift (IS) of 0.00 mm/s for one sextet, indicative of bulk α-Fe. The relative area of the second metal sextet always corresponded to a nominal thickness of 1.8(1) Å of metal per metal/oxide interface and had an "interfacially" enhanced [20] HF (350 kOe) and IS (∼0.05 mm/s). The fractional contribution of these two subspectra to the total spectral area was taken as f. The nominal thickness of metal oxidized per layer, $t_{\rm ox} = (1-f)t_0$, was independent of t_0 and averaged 8.4(2) Å.

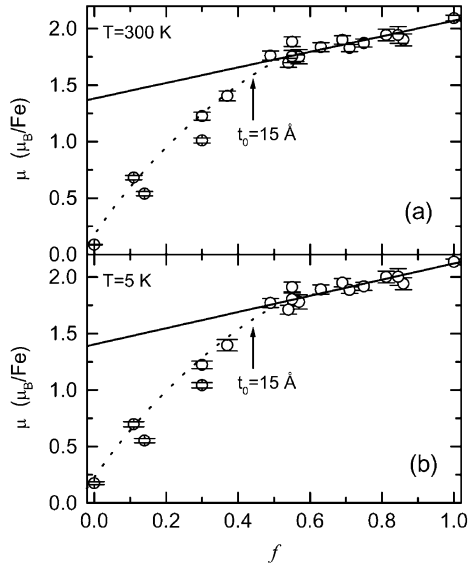

Fig. 6. Average net moment versus metal fraction for a series of $[{\rm Fe}(t_0)/{\rm natox}]_N$ MNOMs measured at (a) 300 K and (b) 5 K. Intercepts at $f = 0$ and $f = 1$ give oxide and metal net moments, respectively, over the fitted range.

Fig. 6(a) shows $\bar{\mu}_{\rm net}$ measured at 300 K as a function of f for these samples. For samples with sufficiently thick metal layers ($f > 0.40$, or $t_0 > 14$ Å), $\bar{\mu}_{\rm net}$ is linear with f. A fit to (11) for $f > 0.40$ yields net moments of 2.1(1) μ_B/Fe and 1.38(6) μ_B/Fe for the metal and oxide, respectively. $\mu_{\rm net}^m$ agrees with the moment of bulk α-Fe, 2.172 μ_B/Fe, while $\bar{\mu}_{\rm net}^{\rm ox}$ has a value close to that of magnetite (Fe_3O_4), 1.35 μ_B/Fe.

Nearly identical data are found at $T = 5$ K, [Fig. 6(b)]. $\mu_{\rm net}^m$ and $\bar{\mu}_{\rm net}^{\rm ox}$ extracted from the linear region each increase by only ∼2% from their 300 K values. This weak temperature dependence, similar to that of bulk α-Fe, indicates that the magnetic native oxide is thermally stable at room temperature and orders at a substantially higher temperature.

Below $f \approx 0.4$, $\bar{\mu}_{\rm net}$ drops precipitously to 0 as $f \to 0$. From (11), this evidently requires $\bar{\mu}_{\rm net}^{\rm ox} \to 0$ as $f \to 0$. The vanishing of $\bar{\mu}_{\rm net}^{\rm ox}$ is accompanied by a collapse in magnetic hyperfine field (HF) splitting in the CEMS oxide subspectra. Above $f \approx 0.4$, the (room-temperature) Mössbauer oxide subspectra have an average HF splitting of ∼310 kOe, with 70% of the spectrum narrowly distributed around ∼380 kOe and the remainder broadly distributed at lower HFs [19]. The HF distribution is independent of f for $f > 0.4$, but the HF splitting drops as $f \to 0$ below this threshold. In the limit of $f = 0$, realized for $t_0 = 5$ Å, the oxide CEMS spectrum is a nonmagnetic doublet characteristic of paramagnetic (nonstoichiometric) FeO. There is thus a critical thickness $t_0^{\rm crit} \approx 15$ Å, above which the native oxide magnetic characteristics are invariant, but below which the oxide

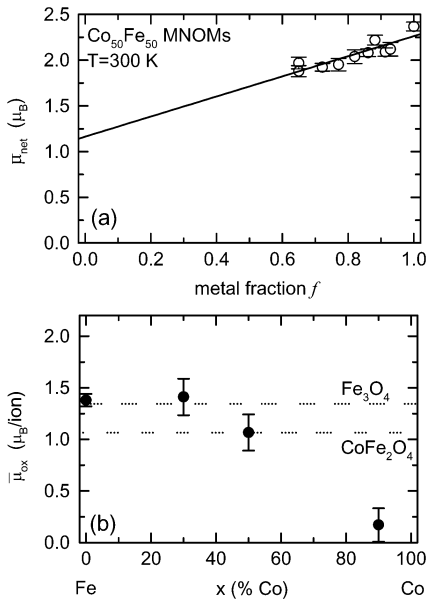

Fig. 7. (a) Average net moment versus metal fraction for a series of $[Co_{50}Fe_{50}(t_0)/natox]_N$ MNOMs measured at 300 K. (b) Room-temperature net moment per transition metal ion for the buried native oxide in MNOMs of several compositions.

magnetism depends critically on the metal thickness. The magnetism of the buried native oxide is stabilized by the proximate Fe metal, and collapses in the absence of the metal.

The large net moment of the (magnetic) buried native Fe oxide is preserved with the addition of at least 50% Co. The average room-temperature net moment $\bar{\mu}_{\rm net}$ versus f for a series of $[Co_{50}Fe_{50}(t_0)/natox]_N$ films with t_0 from 20 to 100 Å is shown in Fig. 7(a). $t_{\rm ox} = 7(1)$ Å was measured for a $[Co_{50}Fe_{50}(20$ Å$)/natox]_{50}$ in [10]. This value was assumed to be independent of t_0, as was measured for the Fe MNOMs, and was used in calculating f for the remaining samples. The moment data are again linear in f. The slope and intercept as given by (11) yield $\mu^m_{\rm net} = 2.3(3)\ \mu_B$ and $\bar{\mu}^{\rm ox}_{\rm net} = 1.2(2)\ \mu_B$ per transition metal atom (or ion). As for the native Fe oxide, the net moment of the $Co_{50}Fe_{50}$ native oxide shows only a weak temperature dependence, with nearly identical data to those of Fig. 7(a) observed at $T = 5$ K.

The data of Figs. 6 and 7 indicate that the net moment of the metal is the bulk value in $x = 0$ and $x = 50$ MNOM films. By assuming bulk moments for the metallic component in MNOM films of other compositions, the net oxide moment has been determined using (11) for several additional samples through measurements of f and $\bar{\mu}_{\rm net}$. Using the measured metal fraction [10] and net moment $\bar{\mu}_{\rm net}$ for $[Co_{30}Fe_{70}(20$ Å$)/natox]_{50}$ and $[Co_{90}Fe_{10}(20$ Å$)/natox]_{50}$ films, the net moment of the native oxide was determined for these compositions. The variation of $\bar{\mu}^{\rm ox}_{\rm net}$ with alloy composition is summarized in Fig. 7(b) for $x = 0, 30, 50$, and 90. The data show little change in the average net moment of the native oxide up to at least $x = 50$. However, $\bar{\mu}^{\rm ox}_{\rm net}$ drops considerably at high Co fraction $(x = 90)$. This decrease is accompanied by diminished magnetic HF splitting for the oxidized Fe [10], [21].

The reason for the falloff in oxide magnetism in the Co-rich native oxide is unclear. We note that X-ray diffraction and EXAFS results [10] indicate a crossover in the metallic crystal structure from bcc for $x < 90$ to fcc at $x \geq 90$ for these samples, consistent with the bulk Co_xFe_{100-x} phase diagram [14]. It is possible that the Fe-rich magnetic native oxides are partially stabilized by local epitaxial constraints induced by the metal, which would change with a change in the metal crystal structure. Notably, the loss of magnetism in the native oxide coincides with the loss of soft magnetic properties in the composite [19].

B. Magnetization

From an applications perspective, it is not the net moment but rather its volume average, i.e., the magnetization, that is important. It is therefore necessary to determine the volume expansion due to oxidation in the MNOM system. We proceed as in [19] to determine this oxidation expansion factor in the Fe MNOM system.

In $[Fe(t_0)/natox]_N$, the metal/native oxide bilayer thickness Λ is larger than t_0 due to the oxidation and subsequent expansion of a fraction $(1 - f)$ of the Fe by a factor α (shown schematically in Fig. 8). In each bilayer, a nominal thickness $t_{\rm ox} = (1 - f)t_0$ of Fe oxidizes, leaving a metal layer of nominal thickness $t_m = ft_0$. With $\Lambda = t_m + \alpha t_{\rm ox}$, the total volume expansion due to oxygen incorporation for a MNOM, Λ/t_0, is determined *solely* by α and f via

$$\frac{\Lambda}{t_0} = \alpha + (1 - \alpha)f. \tag{12}$$

It is therefore possible to determine α for the buried native oxide layers by measuring only the total volume and the metal atomic fraction for a MNOM.

X-ray reflectivity (XRR) accurately yields the total MNOM thickness $N\Lambda$ or, equivalently, Λ, and Mössbauer spectroscopy provides the metal fraction f. In Fig. 8(c), Λ/t_0 versus f for a series of MNOMs falls on a single line of constant α; each oxidized Fe ion requires an average volume greater by a factor $\alpha = 1.51(4)$ than the Fe metal atoms in a bcc lattice, due to the incorporated O^{2-}.

The average net moment of the buried native Fe oxide is 1.38(6) μ_B/Fe at room temperature. This value is close to the bulk net moments of the ferrimagnetic Fe oxides γ-Fe_2O_3 (1.15 μ_B/Fe) and Fe_3O_4 (1.35 μ_B/Fe). However, a given volume of Fe metal must expand by a factor of at least $\alpha = 2.1$ when oxidized to Fe_3O_4 and by $\alpha = 2.33$ to form γ-Fe_2O_3 [19], to accommodate the O^{2-} required to coordinate the Fe ions. Because the moment-bearing Fe ions in the native Fe oxide layers have a substantially higher packing density than those in the spinel Fe oxides, the effective magnetization (i.e., moment density) is correspondingly larger. The native oxide contributes a magnetization of 732(35) emu/cm^3 to an Fe MNOM, a value 42(6)% larger than for Fe_3O_4 and 89(8)% larger than for γ-Fe_2O_3. Thus, the magnetization of the buried native Fe oxide exceeds that of any other Fe oxide system.

C. Stoichiometry

The measured oxidation expansion leads, upon closer inspection, to an unexpected result: the expansion is insufficient to accommodate any more than $\sim$1 O^{2-} ion per oxidized Fe ion,

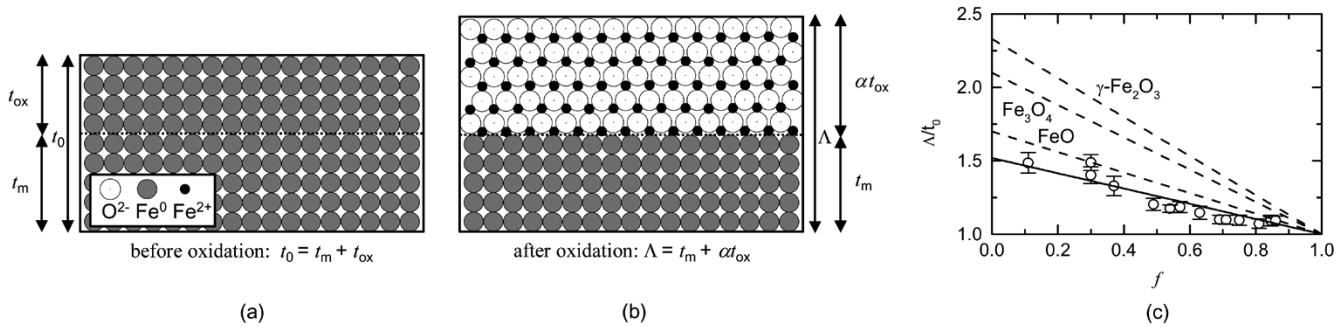

Fig. 8. Schematic of metallic Fe layer (a) before oxidation and (b) after oxidation, indicating notation for nominal layer thicknesses. The nominal layer thicknesses are drawn to scale with those observed in $[\mathrm{Fe}(20\ \text{Å})/\mathrm{natox}]_{50}$, based on the measured atomic metal fraction f and total bilayer thickness Λ, and the ionic radii are scaled accordingly. (c) Measured volume expansion versus metal atomic fraction for a series of $[\mathrm{Fe}(t_0)/\mathrm{natox}]_N$ films (symbols) and linear fit (solid line). Dashed lines indicate expansion expected for the indicated oxide phases.

implying a predominantly Fe^{2+} native oxide. This conclusion is motivated by considering the minimum volume required by a metal/oxide composite of a given metal fraction and oxide stoichiometry.

Because the ionic volume of O^{2-} is ~10–20 times greater than those of Fe $^{2+}$ and Fe^{3+} [22], the volume of an Fe oxide depends only on the quantity and packing density of the incorporated O^{2-}. The O^{2-} ions form a close-packed fcc lattice that is nearly identical for all the cubic (bulk) Fe oxides (FeO, Fe_3O_4, and γ-Fe_2O_3), with an O^{2-}-O^{2-} spacing limited by the O^{2-} ionic radius. The much smaller Fe ions occupy interstitial sites and only minimally perturb the O^{2-}-O^{2-} spacing. Thus, the O^{2-} packing density is near its upper limit in these bulk Fe oxides. The quantity of O^{2-} necessary to coordinate a given quantity of ionic Fe, and thus the minimum total volume of that O^{2-}, is proportional to the average valence of the Fe, and ranges from 1 to 1.5 O^{2-} per Fe ion for Fe^{2+} and Fe^{3+}, respectively.

The expansion factor α for the bulk Fe oxides, or the average total volume per Fe ion in the oxide normalized to the average volume per Fe atom in bcc Fe metal, is therefore near the minimum volume expansion required for an oxide of a given valence. α increases linearly with average Fe valence in these bulk oxides, at 1.7, 2.10, and 2.33 for FeO, Fe_3O_4, and γ-Fe_2O_3, respectively. The corresponding α for the native oxide, taken from the data of Fig. 8(c) via (12), averages 1.51(4), and shows no significant change over a wide range of metal fraction in the composite. The discrepancy between the measured expansion and that required for Fe^{3+} corresponds to an average thickness less by 7 Å in every bilayer of every MNOM sample. Given the measured quantities of metallic and ionic Fe via Mössbauer spectroscopy, and the total bilayer thickness (or volume) via X-ray reflectometry, the existence of an Fe^{3+} oxide in, for example, $[\mathrm{Fe}(20\ \text{Å})/\mathrm{natox}]_{50}$, would require the addition of 50% more O^{2-} within the volume indicated schematically in Fig. 8(b). Clearly, no economies of packing could allow for the incorporation of the additional O^{2-} required by a significant fraction of Fe^{3+} in these oxide layers, and the oxide layers must be primarily divalent. In particular, the uncertain metal/oxide interfacial packing density could alter the average bilayer thickness by no more than the O^{2-} radius of 1.4 Å.

The Fe^{2+} valence of the buried native oxide has been confirmed with cross-sectional nanoprobe electron energy loss spectroscopy (EELS) [19], and by the X-ray and nuclear scattering length densities measured using X-ray and polarized neutron reflectometry [21]. We include here further evidence of the native oxide valence, through the experiments of Parker *et al.* [21], [23].

In the bulk Fe-O phase diagram, Fe_3O_4 is the most thermodynamically stable phase in the temperature range ~400 °C–600 °C. This fact suggests that annealing an Fe MNOM may drive the native oxide toward this composition. If the total quantities of O^{2-} and Fe in a MNOM were conserved, such a temperature-driven reaction would proceed as

$$f_i\mathrm{Fe}^0 + (1 - f_i)\mathrm{FeO}_x \rightarrow f_a\mathrm{Fe}^0 + (1 - f_a)\mathrm{FeO}_y. \quad (13)$$

Here, f_i and f_a represent the initial and final atomic fractions, respectively, of Fe in the metallic state (Fe^0). x and y are the average stoichiometries of the oxide before and after the reaction. In any such experiment, Mössbauer spectroscopy can accurately determine f_i and f_a; therefore, if the post-reaction stoichiometry of the oxide could be unambiguously determined, the "unknown" stoichiometry of the as-formed native oxide would be given by

$$x = \frac{(1 - f_a)}{(1 - f_i)}y. \quad (14)$$

Annealing experiments were performed in a quartz tube furnace under flowing high-purity Ar gas. Samples were deposited on thermally oxidized SiO_2(~3000 Å)/Si. These substrates were used to prevent any reaction of Si with Fe or O in the films during annealing. The films were capped with a 100 Å SiO_2 layer to protect from residual oxygen in the annealing furnace. A metallic film, Fe(1000 Å), was prepared in this manner and annealed at 525 °C for 2 h. CEMS spectra before and after annealing were identical and showed no phases other than metallic α-Fe; in particular, there was neither any measurable oxidation during annealing nor any reaction of the Fe with the substrate.

An SiO_2(100 Å)-capped MNOM film, $[\mathrm{Fe}(20\ \text{Å})/\mathrm{natox}]_{50}$, was also prepared on a thermally oxidized Si substrate and annealed at 525 °C for 2 h. The room-temperature CEMS spectrum before annealing [Fig. 9(a)] consists of partially overlapping magnetically split sextets corresponding to metal and oxide subspectra. The data were fitted as described in [19], and the metallic component was identified on the basis of its isomer shift of ~0.0 mm/s.

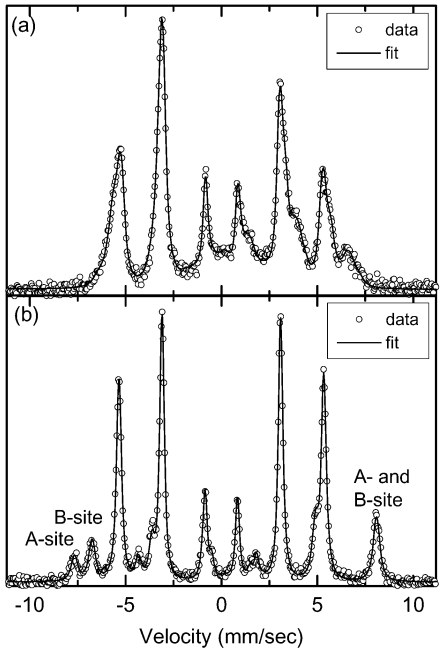

Fig. 9. Room-temperature CEMS spectra of a [Fe(20 Å)/natox]$_{50}$ film as deposited (a) and after annealing at 525 °C for 2 h (b). Lines 1 and 6 of the octahedral (A) and tetrahedral (B) sites in the Fe_3O_4 subspectrum are labeled.

Before annealing, the Mössbauer spectrum of the native oxide does not correspond to any known Fe oxide. However, the Mössbauer spectrum of the annealed MNOM in Fig. 9(b) consists of a sharp metallic sextet and an oxide subspectrum clearly identified as arising from magnetite, Fe_3O_4. The composite spectrum is well-fitted with bulk Fe^0 and Fe_3O_4 subspectra, with no evidence of other phases. X-ray diffraction spectra also contained only peaks consistent with bulk α-Fe and Fe_3O_4 for the annealed film. The relative populations of the octahedral (A) sites and tetrahedral (B) sites, determined from the Mössbauer spectrum, imply a nearly ideal stoichiometry of $Fe_{2.97(2)}O_4$ for this oxide, or $y = 1.34(1)$ in (13).

Based on their relative spectral areas,[1] the metal fractions in this MNOM before and after annealing are 0.55(1) and 0.69(2), respectively. For a fixed total quantity of O^{2-} in the MNOM system before and after annealing, this means that after annealing, there is a larger ratio of O^{2-} to ionic Fe than before; i.e., the quantity of Fe remaining ionic has decreased while its average valence has increased. Using (14), we find that the as-deposited native oxide has an average stoichiometry FeO_x with $x = 0.91(6)$; and hence an average Fe valence of Fe^{2+}.

Thus, despite the large, thermally stable net moment of the buried native Fe oxide (for sufficient metal fraction), it has the stoichiometry of FeO which, in the bulk, is an antiferromagnet with a Néel temperature of 197 K. Though the magnetism of the oxide collapses as the metal fraction decreases to zero, the change in magnetic properties does not appear to be due to a change in stoichiometry [i.e., compare Figs. 6(a) and 8(c)]. Rather, it has been argued [19] that the magnetic oxide is stabilized by exchange with the metal. In the following section, ferromagnetic metal/oxide exchange coupling is explicitly demonstrated.

[1]The bulk Debye temperatures of Fe^0 and Fe_3O_4 differ by ~100 K. Thus, the room-temperature fractional spectral area of the metallic subspectrum, at 0.73(1), slightly overestimates the metal fraction. Correcting for the Debye temperatures gives a metal fraction of 0.69(2). Based on temperature-dependent Mössbauer studies of a Fe MNOM [19], no room-temperature correction is required for the as-deposited metal fraction.

IV. Coupling in the MNOM System

To explain the low-dispersion uniaxial anisotropy in a MNOM nanoscale composite through the exchange averaging of an anisotropy originating in the oxide component, one must assume that the oxide is magnetic and that the metal and oxide form a strongly exchange-coupled medium. The previous section established the validity of the first supposition; this section deals with the second.

To study interlayer exchange coupling in the MNOM system, several multilayer samples have been prepared on antiferromagnetic underlayers. The existence of interlayer coupling is inferred from the presence or absence of an exchange-mediated bias field in the layers not making direct contact with the antiferromagnet. In these experiments, a 500 Å antiferromagnetic $Ni_{0.5}Co_{0.5}O$(NiCoO; $T_N > 400$ K [24]) underlayer, grown by reactive sputtering in O_2, was used as an exchange-biasing layer. The subsequent room-temperature deposition of the Co_xFe_{100-x} multilayer structures was performed in a static dc magnetic field of ~100 Oe that defined the easy axis and the exchange bias direction.

In a Co_xFe_{100-x}/*oxide*/Co_xFe_{100-x} trilayer deposited on NiCoO, the top Co_xFe_{100-x} layer will exhibit exchange bias if and only if magnetic coupling occurs across the *oxide* layer. We first compare the behaviors of two such trilayers:

1) $Co_{50}Fe_{50}$(30 Å)/SiO_2(14 Å)/$Co_{50}Fe_{50}$(20 Å)/NiCoO (500 Å);
2) $Co_{50}Fe_{50}$(30 Å)/*natox*/$Co_{50}Fe_{50}$(30 Å)/NiCoO(500 Å).

In sample 1, a thin nonmagnetic SiO_2 layer separates two $Co_{50}Fe_{50}$ layers of unequal thicknesses (to facilitate their identification in hysteresis loops). In sample 2, the nonmagnetic SiO_2 layer is replaced with a magnetic native oxide layer, while retaining nominally similar layer thicknesses after oxidation. (Both films were also capped with 100 Å SiO_2 to prevent further oxidation).

Fig. 10 compares the easy-axis room-temperature hysteresis loops of the two samples. For sample 1, two distinct magnetic reversals are visible, corresponding to the independent switching of the two $Co_{50}Fe_{50}$ layers. The bottom $Co_{50}Fe_{50}$(20 Å) layer in the trilayer, distinguished by its relative contribution (40%) to the total magnetization, is exchange baised. Its behavior is nearly identical to that of a single exchange-biased $Co_{50}Fe_{50}$(20 Å) layer, which has the hysteresis loop shown in the inset of Fig. 10(a). The top $Co_{50}Fe_{50}$(30 Å) layer switches symmetrically about zero field, showing no influence of exchange bias. The exchange bias field does not extend beyond the SiO_2(14 Å) barrier, implying the absence of interlayer magnetic between the $Co_{50}Fe_{50}$ layers. This result excludes both direct metal–metal exchange coupling (pinhole coupling), and dipolar "orange peel" [25], [26] or domain wall coupling [27] effects as providing significant coupling across this thin SiO_2 barrier.

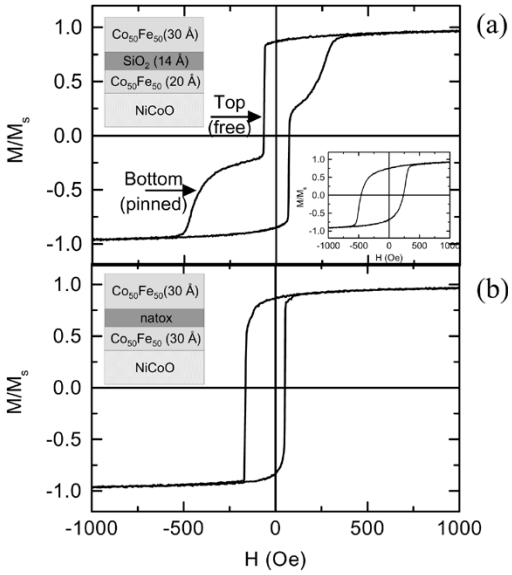

Fig. 10. Hysteresis loops of $Co_{50}Fe_{50}$/*oxide*/$Co_{50}Fe_{50}$ trilayers deposited on antiferromagnetic NiCoO(500 Å), where *oxide* is (a) a nonmagnetic SiO_2(14 Å) layer and (b) a magnetic native oxide layer. CoFe layer thickness are indicated in the schematic insets. A hysteresis loop for a $Co_{50}Fe_{50}$/NiCoO(500 Å) film is shown in the inset of (a).

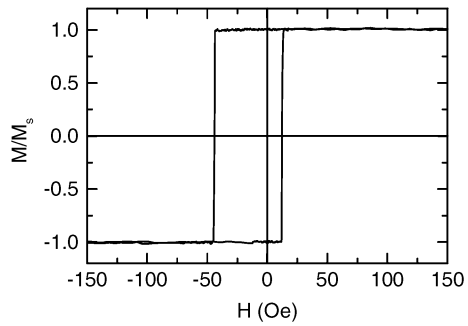

Fig. 11. Hysteresis loops of $[Co_{50}Fe_{50}$(20 Å)/natox$]_{10}$/NiCoO(500 Å).

When the nonmagnetic SiO_2 layer of sample 1 is replaced by a *magnetic* native oxide layer, the behavior is strikingly different. The hysteresis loop of sample 2 in Fig. 10(b) shows a single reversal shifted about zero. This loop demonstrates magnetic coupling between the adjacent metallic layers, both of which experience exchange bias.

TEM images (not shown) of the SiO_2 layer show a low interfacial roughness and no evidence of discontinuities [21]. However, the TEM studies of sample 2 indicated more roughness associated with the native oxide layer, and a lower contrast between the metal and the native oxide made it difficult to confirm oxide continuity in some regions. Therefore, direct metal–metal coupling through pinholes could play a role in interlayer coupling. However, the hysteresis loop of an exchange-biased $[Co_{50}Fe_{50}$(20 Å)/natox$]_{10}$/NiCoO(500 Å) MNOM in Fig. 11 makes clear the existence of exchange coupling *between* the metal and the native oxide. In this film, the native oxide layers contribute ~20% of the total net moment. The hysteresis loop of this exchange-biased MNOM is extremely square, with the entire composite exhibiting the same reversal and exchange-bias fields. Therefore, all layers reverse simultaneously, with interlayer exchange coupling transmitting the exchange-bias field from metal to oxide and from oxide to metal across multiple layers.

V. Conclusion and Outlook

While the promise of the Co_xFe_{100-x} MNOM system for high-permeability, high-frequency applications is clear, many important questions remain. Is it possible to extend the range of soft magnetic properties (low H_c and low-dispersion uniaxial anisotropy) to MNOMs of thicker t_0 ? In the films described in this paper, all metal layers except the initial layer are grown on a thin native Co_xFe_{100-x} oxide layer. If metal grain size refinement is induced by the microstructure of the native oxide underlayers, rather than by a simple periodic interruption of grain growth, then reducing the thickness of the bottommost metal layer in a thick-t_0 MNOM might significantly improve the soft properties of the entire film.

What are the detailed microscopic mechanisms that give rise to the uniaxial anisotropy and its low dispersion? What role does the Fe play in establishing oxide magnetism and soft magnetic properties, which cease to exist above $x = 90$.

Is it possible to achieve net perpendicular anisotropy in MNOMs with sufficiently thin metallic layers? The ability to alternate between in-plane soft magnetic properties and perpendicular anisotropy simply by varying t_0 would be attractive.

Are further enhancements of the oxide magnetization possible? In the case of Fe, the buried native oxide magnetization approaches that of Permalloy. However, it is of a stoichiometry that should have no net moment when ordered, and should not be ordered at room temperature. The reasons for the unusual thermally stable net moment in this largely interfacial native oxide are not yet clear. The ionic moment of Fe^{2+} is $4\mu_B$, suggesting that a fraction of the ionic spins in the native oxide are oriented in opposition to the net moment in a *ferri*magnetic arrangement. Understanding and controlling the interfacial influences on the native oxide spin structure could lead to further increases in the net polarization, bringing it closer to *ferro*magnetic, with the $4\mu_B$ of Fe^{2+}. Such an enhancement would have important implications: the magnetization of ferromagnetic FeO would exceed that of metallic Fe [19].

What are the effects of annealing at the more moderate temperatures common to recording head processing, and what are the properties of the metal/spinel oxide composite that result from high-temperature annealing? The answers to these and other questions would benefit the understanding of this rich material system, and may lead to other fundamentally interesting and technologically important results.

Acknowledgment

This work was supported in part by the National Institute of Standards and Technology's Nanotechnology Initiative. The authors gratefully acknowledge important experimental contributions to this work by P. A. Crozier, M. R. Fitzsimmons, V. G. Harris, F. T. Parker, B. Ramadurai, T. J. Silva, S. K. Sinha, and D. J. Smith, and fruitful discussions with F. E. Spada, E. P. Price, and M. F. Hansen. They also thank the referees of this paper for helpful suggestions.

REFERENCES

[1] G. S. D. Beach, A. E. Berkowitz, F. T. Parker, and D. J. Smith, "Magnetically-soft, high-moment, high resistivity thin films using discontinuous metal/native oxide multilayers," *Appl. Phys. Lett.*, vol. 79, pp. 224–226, May 2001.

[2] G. S. D. Beach, T. J. Silva, F. T. Parker, and A. E. Berkowitz, "High-frequency characteristics of metal/native-oxide multilayers," *IEEE Trans. Magn.*, vol. 35, no. 5, pp. 2669–2671, Sep. 2003.

[3] G. S. D. Beach and A. E. Berkowitz, "Co–Fe metal/native-oxide multilayers: A new direction in soft magnetic thin film design I. Quasistatic properties and dynamic response," *IEEE Trans. Magn.*, vol. 41, no. 6, pp. 2043–2053, Jun. 2005.

[4] C. L. Platt, A. E. Berkowitz, D. J. Smith, and M. R. McCartney, "Correlation of coercivity and microstructure of thin CoFe films," *J. Appl. Phys.*, vol. 88, pp. 2058–2062, Aug. 2000.

[5] M. Ohnuma, K. Hono, H. Onodera, S. Ohnuma, H. Fujimori, and J. S. Pedersen, "Microstructure and magnetic properties of Co-Al-O granular thin films," *J. Appl. Phys.*, vol. 87, pp. 817–823, Jan. 2000.

[6] S. Ohnuma, N. Kobayashi, T. Masumoto, S. Mitani, and H. Fujimori, "Magnetostriction and soft magnetic properties of $(Co_{1-x}Fe_x)$-Al-O granular films with high electrical resistivity," *J. Appl. Phys.*, vol. 85, pp. 4574–4576, Apr. 1999.

[7] J. Huijbregtse, F. Roozeboom, J. Sietsma, J. Donkers, T. Kuiper, and E. van de Riet, "High-frequency permeability of soft-magnetic Fe-Hf-O films with high resistivity," *J. Appl. Phys.*, vol. 83, pp. 1569–1571, Feb. 1998.

[8] T. Morikawa, M. Suzuki, and Y. Taga, "Soft magnetic properties of Co-Cr-O granular films," *J. Magn. Soc. Jpn.*, vol. 23, pp. 234–239, 1999.

[9] Y. Chen, S. Hossain, C. Qian, M. Miller, and H.-C. Tong, "FeTaN films with ultrafine grain structure," *J. Appl. Phys.*, vol. 85, pp. 4562–4564, Apr. 1999.

[10] G. S. D. Beach, V. G. Harris, F. T. Parker, B. Ramadurai, D. J. Smith, and A. E. Berkowitz, "Properties of the native oxide in metal/native oxide multilayers," *J. Appl. Phys.*, vol. 91, pp. 7526–7528, Jun. 2002.

[11] G. Herzer, "Grain size dependence of coercivity and permeability in nanocrystalline ferromagnets," *IEEE Trans. Magn.*, vol. 26, no. 5, pp. 1397–1402, Sep. 1990.

[12] H. Hoffman, "Influence of local inhomogeneities on the magnetic properties of thin ferromagnetic films and nanostructures," *Thin Solid Films*, vol. 373, pp. 107–112, 2000.

[13] S. Chikazumi, *Physics of Ferromagnetism*, 2nd ed. Oxford, U.K.: Clarendon, 1997.

[14] K. Hellwege, Ed., *Landölt-Bornstein*. Berlin, Germany: Springer-Verlag, vol. 19a. Group III.

[15] J. Slonczewski, "Origin of magnetic anisotropy in cobalt-substituted magnetite," *Phys. Rev.*, vol. 110, pp. 1341–1348, Feb. 1958.

[16] H. S. Jung, W. D. Doyle, and S. Matsunuma, "Influence of underlayers on the soft properties of high magnetization FeCo films," *J. Appl. Phys.*, vol. 93, pp. 6462–6464, May 2003.

[17] B. N. Engel, C. D. England, R. A. Van Leeuwen, M. H. Wiedmann, and C. M. Falco, "Interface magnetic anisotropy in epitaxial superlattices," *Phys. Rev. Lett.*, vol. 67, pp. 1910–1913, Sep. 1991.

[18] J. L. Snoek, "Dispersion and absorption in magnetic ferrites at frequencies above one Mc/s," *Physica*, vol. 14, pp. 207–217, May 1948.

[19] G. S. D. Beach, F. T. Parker, D. J. Smith, P. A. Crozier, and A. E. Berkowitz, "New magnetic order in buried native iron oxide layers," *Phys. Rev. Lett.*, vol. 91, p. 267201, Dec. 2003.

[20] T. Shinjo, T. Iwasaki, T. Shigematsu, and T. Takada, "Mossbauer studies of very thin oxide layer on Fe surface," *Jpn. J. Appl. Phys.*, vol. 23, pp. 283–285, Mar. 1984.

[21] G. S. D. Beach, "The CoFe metal/native oxide multilayer," Ph.D. thesis, Univ. California, San Diego, 2003.

[22] *CRC Handbook of Chemistry and Physics*, 83rd ed., D. R. Lide, Ed., CRC, Boca Raton, FL, 2002.

[23] F. T. Parker, G. S. D. Beach, and A. E. Berkowitz, "Determining the buried native FE oxide stoichiometry through annealing," unpublished.

[24] M. J. Carey and A. E. Berkowitz, "Exchange anisotropy in coupled films of NiFe with NiO and CoNiO," *Appl. Phys. Lett.*, vol. 60, pp. 3060–3062, Jun. 1992.

[25] L. Néel, *Comptes Rendus*, vol. 255, p. 1676, 1962.

[26] J. C. S. Kools, W. Kula, D. Mauri, and T. Lin, "Effect of finite magnetic film thickness on Néel coupling in spin valves," *J. Appl. Phys.*, vol. 85, pp. 4466–4468, Apr. 1999.

[27] C. L. Platt, M. R. McCartney, F. T. Parker, and A. E. Berkowitz, "Magnetic interlayer coupling in ferromagnet/insulator/ferromagnet structures," *Phys. Rev. B, Condens. Matter*, vol. 61, pp. 9633–9641, Apr. 2000.

Manuscript received September 29, 2004; revised February 17, 2005.